Human Brain Mapping

WILEY

Constrained principal component analysis reveals functionally connected load-dependent networks involved in multiple stages of working memory

scholarONE™
Manuscript Central

CPCA 1

Constrained principal component analysis reveals functionally connected load-dependent networks

involved in multiple stages of working memory

Paul Metzak[1,2], Eva Feredoes[3], Yoshio Takane[4], Liang Wang[1,2], Sara Weinstein[1,2],

Tara Cairo[2], Elton T.C. Ngan[1], & Todd S. Woodward[1,2*]

[1]Department of Psychiatry, University of British Columbia, Vancouver, BC, Canada.

[2]BC Mental Health and Addictions Research Institute, Vancouver, BC, Canada.

[3]Institute of Cognitive Neuroscience, University College London, London, United Kingdom.

[4]Department of Psychology, McGill University, Montreal, PQ, Canada.

* Corresponding Author. Please address all correspondence to: Todd S. Woodward, Ph. D., Room A3-A116, BC Mental Health & Addictions Research Institute – Translational Research Building, 3rd Floor, 938 W. 28th Avenue, Vancouver, British Columbia, Canada, V5Z 4H4, fax: 604-875-3871, phone: 604-875-2000 x 4724, e-mail: Todd.S.Woodward@gmail.com.

CPCA 2

Abstract

Constrained principal component analysis (CPCA) with a finite impulse response (FIR) basis set was used to reveal functionally connected networks and their temporal progression over a multi-stage verbal working memory trial in which memory load was varied. Four components were extracted, and all showed statistically significant sensitivity to the memory load manipulation. Additionally, two of the four components sustained this peak activity, both for approximately 3 seconds (components 1 and 4). The functional networks that showed sustained activity were characterized by increased activations in the dorsal anterior cingulate cortex, right dorsolateral prefrontal cortex, and left supramarginal gyrus, and decreased activations in the primary auditory cortex and "default network" regions. The functional networks that did not show sustained activity were instead dominated by increased activation in occipital cortex, dorsal anterior cingulate cortex, sensori-motor cortical regions, and superior parietal cortex. The response shapes suggest that although all four components appear to be invoked at encoding, the two sustained-peak components are likely to be additionally involved in the delay period. Our investigation provides a unique view of the contributions made by a network of brain regions over the course of a multiple-stage working memory trial.

Introduction

        Working memory can be described as the ability to hold a limited amount of information in an

active state, for use in guiding behaviour after the information is removed from the environment

(Baddeley and Hitch 1974). A common approach to testing working memory experimentally using

functional magnetic resonance imaging (fMRI) involves the delayed recognition task. Experiments

using delayed recognition involve three stages: (1) encoding, during which items to remember are

presented, (2) delay, during which the previously presented items must be maintained, and (3) probe,

during which a recognition test for the previous items is administered. Functional neuroimaging

investigations often attempt to identify and localize cognitive processes engaged by these individual

task stages.

        One limitation of many such investigations, however, is that the stages are assessed separately

and in isolation to one another. As a result, there is limited knowledge on how the involved brain

regions change over the course of a delayed recognition trial, making inferences on the extent to which

distinct networks of regions contribute separately to each task stage difficult (Postle 2006). In addition,

as has been previously noted (e.g., Cairo, et al. 2004; Manoach, et al. 2003; Woodward, et al. 2006),

attempts to analyze fMRI data by modeling stage-specific working memory processes can lead to a

number of methodological concerns, particularly when stage-specific hemodynamic response functions

(HRFs) are used in prediction models. Due to the assertion of an assumed HRF shape associated with

each specific task stage, the estimated blood oxygen level-dependent (BOLD) response for any given

stage is, by virtue of the application of multiple regression, restricted to a scaled version of the model's

shape. Because there is substantial overlap between the HRF modeled for each task stage, and because

these stages necessarily occur in a fixed order, any mismatches between the model and the "true"

evoked BOLD signal shape for that stage is likely to result in an automatic, statistically induced

misattribution of signal to the incorrect task stage. For example, any encoding-specific BOLD

signal that is not fit well by the encoding-labeled HRF model (e.g., more prolonged than expected) may

be fit by the delay-labeled model, and would therefore be automatically misattributed to the delay stage

by the statistical procedure (see Manoach, et al. 2003, for a simulation of this misattribution risk).

Moreover, highly correlated predictors in multiple regression are associated with inflated standard

errors (Pedhazur 1982, p. 245), resulting in unstable parameter estimates. Although important advances

have been made regarding how some of these problems can be avoided by adjusting the timing of the

experimental design (Ollinger, et al. 2001) and placement of impulse response functions in the HRF

model (Zarahn, et al. 1997), in addition to sometimes requiring potentially undesirable changes to the

behavioral task paradigm, this area of research is still susceptible to interpretative errors caused by

labeling potentially inaccurate hemodynamic response models of task stages. This is a particularly

pertinent point for delayed recognition tasks, for which an assumed shape of evoked responses is

important for interpreting whether or not a region is involved in a particular task stage (e.g., sustained

delay period activity reflecting storage- and maintenance-related processes; Postle, et al. 2000).

Data analytic approaches that focus on peristimulus time (i.e., on the time points immediately

following, or preceding and following, presentation of the imperative stimulus) instead of isolated task

stages avoid the interpretational errors associated with automatic misattribution of signal to the incorrect

task stage. Using a deconvolution approach focusing on peristimulus time, minimal assumptions are

made regarding the shape of evoked responses of interest (Dale and Buckner 1997; Glover 1999). Thus,

unlike modeling task stages with synthetic HRF models, this method does not impose the assumption

that the brain processes involved in working memory are organized according to the discrete stages of

the behavioral task. One of the simplest and least constrained approaches to deconvolution is the finite

impulse response (FIR) approach, which provides an estimate of average BOLD response amplitude for

a number of peristimulus time points (Henson, et al. 2001; Serences 2004). A univariate FIR model

approach has previously been employed in a working memory study (Manoach, et al. 2003), but such an

analysis produces images of neural activation computed separately for each peristimulus time

point, and so difficulties arise in formally selecting the "correct" time points for further inspection, and

as a result, also in determining the progression of activation change over peristimulus time points.

In contrast to univariate methods, multivariate analyses methods using a FIR model can extract

patterns of intercorrelation among voxels that are determined by, and can be mapped back to,

coordinated changes in BOLD signal over peristimulus time, thereby allowing estimated changes in

activation in a single neural network to be followed over peristimulus time. Several methods exist which

permit this, but if functional connectivity is to be approached in a whole-brain exploratory fashion,

whereby any voxel could potentially load onto the network, then methods which involve a priori

specification of specific regions of interest, such as dynamic causal modeling or structural equation

modeling (Penny, et al. 2004), are not suitable. A number of exploratory multivariate methods are

available. Some, such as principal component analysis (Viviani, et al. 2005) and independent

component analysis (ICA; McKeown, et al. 1998) do not take into account information about the

stimulus timing prior to computing the neural networks (it should be noted that ICA methods are now

being developed that allow this; Calhoun, et al. 2005). Other exploratory methods incorporate

information about stimulus timing into the computations prior to extracting patterns of intercorrelation,

and focus on summarizing the patterns of inter-relationship between two sets of variables (the obtained

BOLD data and the model). Examples of these model-based methods are partial least squares (PLS;

McIntosh, et al. 2004), canonical variates analysis (CVA; Strother, et al. 2004), and multivariate linear

models method (MLM; Worsley, et al. 1997). In the current study we use an approach that falls into this

model-based category, referred to as FIR-based constrained principal component analysis (FIR-CPCA;

http://www.nitrc.org/projects/fmricpca). More detail about how FIR-CPCA compares to other methods

that decompose inter-relationships between two sets of variables will be presented in the Discussion

section.

In the current study we employed FIR-CPCA to visualize, across multiple subjects, how

functional networks change over the course of a multi-stage behavioral trial (i.e., over peristimulus

time), and how these networks respond to experimental manipulations. Using a variable memory load

delayed-recognition data set, we demonstrate how this approach allows (1) the determination of

multiple functional networks involved in working memory, (2) the estimation of the pattern of BOLD

changes associated with each functional network over the course of a trial, (3) a statistical test of the

reliability of the HRF associated with each component; and (4) a statistical test of the degree to which

experimental manipulations (in this case working memory load) affect each functional network.

Methods

Details regarding the motivation for task design, nature of the sample and data acquisition have

been published previously (Cairo, et al. 2004); a summary is presented here. Subjects were 18 right-

handed, healthy, native English speakers (10 women, mean age 27.50 years, age range 18 - 35). Written

informed consent was obtained prior to participation, and all experimental procedures were approved by

the University of British Columbia's Clinical Research Ethics Board. Subjects performed a variable

load delayed recognition working memory task while undergoing fMRI. During a single trial of this

task, subjects viewed a string of 2, 4, 6 or 8 differing uppercase consonants for 4 s, which they were

instructed to remember over a short delay. Following the delay, a single lowercase consonant was

shown for 1 s. Subjects were asked to decide whether this letter had been included in the preceding

letter string. Binary responses were indicated by right-handed index and middle finger presses, and the

finger-response assignments were counterbalanced across subjects. The probe stage was followed by an

inter-trial interval of 3, 4 or 5 s in duration. 20% of the experimental trials were followed by a blank

trial of similar length in which the world "Relax" was projected on the screen. The jittering of the delay

phase and the inter-trial interval, and the blank trials, were implemented to in order to optimize the

experimental design according to available recommendations (Dale 1999).

Echo-planar images were collected on a standard clinical GE 1.5 T system fitted with a

Horizon Echo-speed upgrade. Conventional spin-echo T1 weighted sagittal localizers were used to view

the positioning of the participant's head and to graphically prescribe the functional image volumes.

Functional image volumes were collected with a gradient echo (GRE) sequence (TR/TE 3000/40 ms, 90

flip angle, FOV 24×24 cm, 64×64 matrix, 62.5 kHz bandwidth, 3.75×3.75 mm in plane resolution, 5.00

mm slice thickness, 29 slices, 145 mm axial brain coverage). Each stimulus run consisted of 194 scans

(encompassing the entire brain). The first 12 s (4 scans) collected at the beginning of each run were

discarded, to avoid variation due to T1 saturation effects. Functional images were reconstructed offline.

Statistical parametric mapping software (SPM2, Wellcome Institute of Cognitive Neurology, London,

UK, http://www.fil.ion.ucl.ac.uk/spm) was used for image realignment and normalization into Montreal

Neurological Institute (MNI) anatomical space (resampled to 4 x 4 x 4 mm voxel sizes), and spatially

smoothed using a Gaussian kernel (8 mm FWHM).

Constrained Principal Component Analysis

Most fMRI experiments are designed to determine how stimulus presentations cause BOLD

signal to change; therefore, from this perspective, information about the stimulus presentations should

be considered a set of predictor variables, and the BOLD signal a set of criterion variables. A

multivariate analysis method that takes this conceptual framework into consideration is constrained

principal component analysis (CPCA; Takane and Shibayama 1991). CPCA is a general method for

structural analysis of multivariate data that combines regression analysis and principal component

analysis into a unified framework. As for typical principal component analysis on fMRI data, this

method derives images of functional neural networks from singular-value decomposition of BOLD

signal time series; however, CPCA allows derivation of images when the analyzed BOLD signal is

constrained to that aspect of variance in BOLD signal predictable from how the stimuli were presented.

We now briefly present the matrix equations for the current application of CPCA (for the

comprehensive CPCA theory and proofs please see Hunter and Takane 2002; Takane and Hunter 2001;

Takane and Shibayama 1991). This involves preparation of two matrices. The first matrix contains

columns of normalized and smoothed subject-mean-centered BOLD time series (i.e., activations) for all

voxels over all scans for all subjects, stacked vertically: Z. The second matrix, G, can be referred to as

the *design matrix*. It contains models of the expected BOLD response to the timing of stimulus

presentations. The matrix of BOLD time series (Z) and design matrix (G) are taken as input, with

BOLD in Z being predicted from the model in G. In order to achieve this, multivariate least-squares

linear regression is carried out, whereby the BOLD time series (Z) is regressed onto the design matrix

(G):

$$Z = GC + E , \qquad\qquad (1)$$

where $C = (G'G)^{-1}G'Z$. This analysis yields condition-specific regression weights in the C matrix (i.e.,

regression weights specific to the experimental conditions as defined by the design matrix). The

condition-specific regression weights are often referred to (in conventional fMRI analyses) as beta

images. GC contains variability in Z that is predictable from the design matrix G, that is to say,

variability in Z that is predictable from an idealized BOLD response to the timing of stimulus

presentation.

The next step involves extracting a component (or components) that represents a network (or

networks) of functionally interconnected voxel activations that are related to the experimental stimulus

presentations. This involves singular value decomposition of the activation variability that was

predictable from the design matrix (GC). The maximum number of extractable components is equal to

the rank of GC, which is the minimum row or column subscript of G:

$$UDV' = GC , \qquad\qquad (2)$$

where U = matrix of left singular vectors; D = diagonal matrix of singular values; V = matrix of right singular vectors. Each column of V can be overlaid on a structural brain image to allow visualization of the neural regions involved in each functional network. In the current application of CPCA, we orthogonally rotated and rescaled (by D) the V matrix prior to display, so that a rotated *loading matrix* (VD) is displayed. The values of the loading matrix are weights that represent the contribution of each component (functional network) to the variance of each column of GC, and can be scaled to contain the correlations between the components in U and the variables in GC.

To interpret the components with respect to the conditions represented in G, we produced predictor weights (Hunter and Takane 2002) in matrix P. These are the weights that would be applied to G to create U ($U=G*P$). They indicate the importance of each column in the G matrix to the network(s) represented by the component(s), so are essential for relating the resultant components to the experimental conditions of interest represented in G.

Preparation of Z and G

To prepare the Z matrix for the current data, SPM2 was first used to realign, spatially normalize and smooth BOLD data. A binary brain mask image obtained from a fixed-effects SPM2 analysis was used to extract the BOLD signals in 23,929 voxels from each of 190 scans data collected from each individual subject. This produced a matrix of BOLD signals consisting of 3420 rows (18 subjects $\times$ 190 scans) and 23,929 columns. Then the matrix Z was standardized to have zero mean and unit standard deviation in each column for each subject.

In the analysis reported here, the G (design) matrix consisted of a FIR basis set, as opposed to the HRF model employed in past studies (Cairo, et al. 2004; Cairo, et al. 2006; Woodward, et al. 2006). The FIR model estimates the change in BOLD signal at specific peristimulus scans relative to all other scans. The value 1 is placed in rows of G for which BOLD signal amplitude is to be estimated, and the value 0 in all other rows (resulting in "mini boxcar" functions). The time points coded by this model

were the 1st to 8th repetition times (TR) following stimulus presentation. Since the TR for these

data was 3s, this resulted in estimating BOLD signal over a 24s window, with the start of the first time

point (time = 0) corresponding to encoding stimulus onset. Thus, the encoding, delay and probe stages

were not modeled separately; rather, all stages are covered by this 24 s window of peristimulus time.

The columns in this subject-and-condition based G matrix code 8 peristimulus time points for each of

four load conditions (2, 4, 6 and 8 letters), for each subject, totaling 576 columns ($8 \times 4 \times 18 = 576$).

The matrix equations for FIR-CPCA using the matrix dimensions for the current study (and extracting 4

components as in the present study) would then be:

$$_{3420}Z_{23929} = {_{3420}G_{576}C_{23929}} + {_{3420}E_{23929}} \ , \qquad\qquad (3)$$

$$_{3420}U_4 D_4 V'_{23929} \approx {_{3420}G_{576}C_{23929}} \ . \qquad\qquad (4)$$

The columns of G represent points in peristimulus time for each condition and subject combination;

therefore, the predictor weights in $_{576}P_4$ ($_{3420}U_4 = {_{3420}G_{576}P_4}$) are the values that determine the

contribution of each peristimulus time point, for each condition and subject, on the temporal variation in

the functional networks over scans. These predictor weights are therefore appropriate for use in familiar

tests of statistical significance, such as analysis of variance (ANOVA; see below).

Since the sign of a singular vector is arbitrary, positive values in the loading matrix (VD) do not

necessarily imply activation increases. Therefore, in order to ensure correspondence between the

interpreted directionality of the hemodynamic response represented by the predictor weights and

activation increases/decreases, for each component, the trial-averaged BOLD signal contained in Z was

extracted for the voxels showing the most extreme 5% of component loadings, and this was displayed

separately for positive and negative component loadings.

Statistical Test of Load Dependence

For each component, predictor weights were produced for each combination of peristimulus

scan, load condition, and subject. These weights can be used to statistically test the effect of

peristimulus time, to determine whether or not the values in the *P* matrix are reflecting a

hemodynamic response and not varying randomly around zero. The effect of increasing memory load

can also be tested, as can a significance test for an interaction between peristimulus time and load.

Leaving out the first point of peristimulus time (which was adjusted to zero for predictor weights in all

conditions for the purposes of display and data analysis), this analysis would be carried out as a 7×4

within-subjects ANOVA for each component, with the factors of Time Point (time points 2-8 after the

initiation of a task trial) and Load (2, 4, 6 and 8 letters) as the within-subject factors. Tests of sphericity

were carried out for all ANOVAs. Greenhouse-Geisser adjusted degrees of freedom are reported when

violations of sphericity affected interpretation of results; otherwise, the original degrees of freedom are

reported.

Component Rotation

Component rotations provide interpretational frameworks with which to understand the data

configuration. Infinite rotations are possible, and rotation choice is up to the discretion of the

investigator. Any of the three (optionally rescaled) matrices that result from this application of CPCA

can be rotated (i.e., *VD*, *U*, or *P*); however, the transformation matrix that is used for the rotation of

either *VD*, *U*, or *P* must also be applied to the other two matrices to ensure that all three matrices are

aligned to the same orientation. In our previous work (Woodward, et al. 2006) we employed promax

rotation to *VD*, and subsequently applied the same transformation to *U* and *P*. Promax rotation is based

on methods such as varimax and quartimax which are oriented towards finding simple structure

(Harman 1967, p. 304; Yates 1987 p. 32), and therefore utilizes the criterion of maximizing the (row-

wise or column-wise) variance of the squared loadings (i.e., voxel-based component loadings, or *VD*).

However, with the current FIR-based application of fMRI-CPCA, our interpretation of components

(with respect to the conditions represented in *G*) is based not on the voxel-based matrix *VD*, but on the

hemodynamic response shape of the predictor weights contained in *P*; therefore, it was logical to apply

rotation to *P* for computation of a transformation matrix, and then apply this transformation

matrix to *VD* and *U*.

The simple-structure criteria that are traditionally used on *VD* would not be appropriate for

application to *P*, because *P* is hypothesized to reflect an HRF shape, not polarization of zero and

nonzero values. One strategy for rotation of *P* is to use a Procrustes-style rotation of *P* to a target matrix

(of the same dimensionality) that represents the HRF shape expected from the experimental design. This

would allow the components to reflect an HRF shape where one is present in the predictor weights,

without limiting the predictable variance to specific shapes (and the task stage labels associated with

them). However, this method does not allow multiple components to be oriented to various

manifestations of the same basic HRF shape, because the computation requires the target matrix in a

Procrustes rotation be of full rank, disallowing repeated shapes in the target matrix. Our rotation

approach involved iteratively generating random Gram-Schmidt orthogonalized transformation matrices

(*T*), applying them to *P*, and selecting the *PT* matrix that most closely matched any of a set of HRF

shapes expected to result from the experimental design. The *T* matrix that resulted from this iterative

method was then applied to the other matrices as follows: $UT = GPT$; VDT ; in order to align them to

the same orientation as *PT*. These matrix equations with row and column subscripts matching the

current analysis are:

$$_{576}P^{*}{}_{4} =\, _{576}P_{4}T_{4} \, , \qquad\qquad (5)$$

$$_{3420}U^{*}{}_{4} =\, _{3420}U_{4}T_{4} =\, _{3420}G_{576}P_{4}T_{4} \, , \qquad\qquad (6)$$

$$_{23929}(VD)^{*}{}_{4} =\, _{23929}V_{4}D_{4}T_{4} \, , \qquad\qquad (7)$$

where P^{*} = rotated *P* matrix; U^{*} = rotated *U* matrix; and $(VD)^{*}$ = rotated *VD* matrix.

The steps for optimizing *T* for rotation of *P* are detailed below:

(1) candidate HRF shapes are repeated for all subjects and all conditions, and as such, populate

vectors having the same number of rows as *P*;

(2) a transformation matrix T is randomly generated and Gram-Schmidt orthogonalized,

and P^* is computed;

(3) the absolute value of Pearson's correlation coefficient is computed between each column of

P^* and each candidate HRF shape vector;

(4) the product of the maximum values derived for each column of P^* is computed;

(5) steps 2-4 are iteratively repeated, with the transformation matrix T that maximizes the

product computed at step 4 retained as the optimal solution.

In the current study, we used 500,000 iterations with a set of 6 candidate HRF shapes. To

produce the 6 HRF shapes, we used SPM2 to produce single-trial time series based on specific task

stages predicted by a canonical HRF, convolved with a delta function. Single and combined event

models were developed for: (1) encoding only; (2) encoding + delay; (3) delay period only; (4) delay +

probe; (5) probe only, and (6) encoding + delay + probe.

Results

Four components were extracted in order to optimize comparison with our previous analysis of

the same data (Woodward, et al. 2006). The percentage of variance in *GC* that was accounted for by

Components 1, 2, 3 and 4 in the unrotated solution was 32.63, 4.71, 2.31, and 1.98, respectively. The

sum of the squared loadings divided by the number of scans for the rotated solution was 20.48, 9.47,

9.01 and 2.66 for Components 1, 2, 3 and 4, respectively. The neural regions comprising the functional

networks represented by each component for FIR-CPCA, and their associated Brodmann's Areas (BAs),

are displayed in Figures 1a-4a, with corresponding anatomical descriptions in Tables 1-4. The mean

predictor weights were plotted as a function of peristimulus time (see Figure 1b-4b), and represent the

response of each functional network to the delayed recognition task at different memory loads.

Component 1. The component loadings mapped onto an M.N.I. structural image, and the

associated predictor weights plotted as a function of peristimulus time, are displayed in Figure 1 and

described in Table 1. The pattern of activity suggests that this functional network involves the

bilateral supramarginal/angular gyri (peaks in BAs 39, 40), with these clusters extending into the

superior temporal gyrus (peak in BA 22) and in the primary auditory cortex (Heschl's Gyrus; peaks in

BAs 41/42 on the left). Other regions important for this component included bilateral superior/middle

frontal gyri (peak in BA 9), and the bilateral posterior cingulate/precuneus (peaks in BA 7, 23).

Inspection of the predictor weights time series combined with the negative component loadings

suggests that, relative to baseline, these regions showed decreased activation at the onset of the trial in a

load-dependent fashion. ANOVA revealed a highly significant Time Point $\times$ Load interaction, $F(18,$

$306) = 15.30$, $p < .001$, $\eta^2 = .47$, suggesting that brain regions in this functional network are sensitive to

increasing memory load. This was due to the magnitude of the Time Point effect increasing from 2 to 4,

6 and 8 letters, $F(6, 102) = 10.72$, $p < .001$, $\eta^2 = .39$; $F(6, 102) = 42.31$, $p < .001$, $\eta^2 = .71$; $F(6, 102) =$

29.00, $p < .001$, $\eta^2 = .63$; $F(6, 102) = 31.06$, $p < .001$, $\eta^2 = .65$, respectively. These significant Time

Point effects demonstrate that the HRF shapes associated with this component were reliable for all load

conditions. Considered within the context of the exclusively negative component loadings in Figure 1a,

inspection of Figure 1c suggests that this pattern of decreased activation relative to baseline was

confirmed with trial-averaged BOLD signal for the regions displayed in Figure 1a.

Component 2. The component loadings mapped onto an M.N.I. structural image, and the

associated predictor weights plotted as a function of peristimulus time, are displayed in Figure 2 and

described in Table 2. This functional network was characterized by activation in bilateral occipital gyri

and primary visual cortex (peaks in BAs 17, 18, 19), bilateral precuneus (peak in BA 7), bilateral

thalamus, bilateral medial/superior frontal gyri and precentral gyri (peaks in BAs 4, 6), and left

postcentral/precental gyrus (peak in BAs 6, 3, 4).

Inspection of the predictor weights time series suggests that relative to baseline, these regions

increased activity at the onset of the trial in a load-dependent fashion, and this was confirmed by

examining the trial-averaged BOLD signal in Figure 2c for the regions displayed in Figure 2a.

An ANOVA carried out on the predictor weights revealed a highly significant Time Point $\times$ Load

interaction, $F(18, 306) = 11.92$, $p < .001$, $\eta^2 = .41$, indicating that the magnitude and/or shape of the

hemodynamic response was dependent on memory load. To interpret this interaction, we studied the

effect of Time Point separately for each load. The magnitude of the Time Point effect increased over

loads of 2, 4, 6 and 8 letters, $F(2.4, 40.8) = 2.71$, $p = .07$, $\eta^2 = .14$; $F(6, 102) = 11.52$, $p < .001$, $\eta^2 = .40$;

$F(6, 102) = 18.37$, $p < .001$, $\eta^2 = .52$; $F(6, 102) = 25.52$, $p < .001$, $\eta^2 = .60$, respectively. These

significant Time Point effects demonstrate that the HRF shapes associated with this component were

reliable for the 4, 6 and 8 letter conditions.

Component 3. The component loadings mapped onto an M.N.I. structural image, and the

associated predictor weights plotted as a function of peristimulus time, are displayed in Figure 3 and

described in Table 3. This functional network was dominated by positive component loadings in the

bilateral occipital gyri and primary visual cortices (BAs 17, 18, 19), bilateral dorsal anterior cingulate

gyri (peaks in BAs 32, 6), right dorsolateral prefrontal cortex (peak in BA 46), and bilateral

supramarginal gyri and superior parietal lobes (peaks in BAs 7, 40).

Inspection of the predictor weights time series suggests that relative to baseline, these regions

increased in activity at the onset of the trial in a load-dependent fashion, and this was confirmed by

examining the trial-averaged BOLD signal in Figure 3c for the regions displayed in Figure 3a. An

ANOVA carried out on the predictor weights revealed a significant Time Point $\times$ Load interaction,

$F(18, 306) = 25.97$, $p < .001$, $\eta^2 = .60$, indicating that the magnitude and/or shape of the hemodynamic

response was dependent on memory load. To interpret this interaction, we studied the effect of Time

Point separately for each load. The magnitude of the Time Point effect increased over loads of 2, 4, 6

and 8 letters, $F(6, 102) = 7.29$, $p < .001$, $\eta^2 = .30$; $F(6, 102) = 5.12$, $p < .001$, $\eta^2 = .23$, $F(6, 102) =$

47.59, $p < .001$, $\eta^2 = .74$; $F(6, 102) = 66.81$, $p < .001$, $\eta^2 = .80$, respectively. These significant Time

Point effects demonstrate that the HRF shapes associated with this component were reliable for

all load conditions.

Component 4. The component loadings mapped onto an M.N.I. structural image, and the

associated predictor weights plotted as a function of peristimulus time, are displayed in Figure 4 and

described in Table 4. This functional network was dominated by positive component loadings in

bilateral medial frontal gyri (peak in BA 6), right dorsolateral prefrontal cortex (peak in BA 46), left

inferior and middle frontal gyrus (peaks in BAs 45, 47), bilateral precentral/postcentral gyri (peaks in

BA 6), and left supramarginal gyrus (peak in BA 40). This component also showed negative component

loadings in the bilateral medial/superior frontal gyri (peaks in BAs 9, 10), bilateral precuneus and

posterior cingulate gyri (peak in BA 23), and bilateral superior temporal activation peaking in the

angular gyri (peaks in BA 39).

Inspection of the predictor weights time series, interpreted alongside the component loadings

displayed on the structural image in Figure 4a, suggests that relative to baseline, some regions increased

and others decreased activation at different points in the working memory trial, in a load-dependent

fashion. An ANOVA carried out on the predictor weights revealed a significant Time Point $\times$ Load

interaction, $F(18, 306) = 3.95, p < .001, \eta^2 = .19$, indicating that the magnitude and/or shape of the

hemodynamic response was dependent on memory load. To interpret this interaction, we studied the

effect of Time Point separately for each load. The magnitude of the Time Point effect increased over

loads of 2, 4, 6 and 8 letters, $F(6, 102) = 6.43, p < .001, \eta^2 = .27; F(6, 102) = 5.36, p < .001, \eta^2 = .24;$

$F(6, 102) = 12.30, p < .001, \eta^2 = .42; F(6, 102) = 17.66, p < .001, \eta^2 = .51$, respectively. These

significant Time Point effects demonstrate that the HRF shapes associated with this component were

reliable for all load conditions. Inspection of Figure 4c and 4d suggests that this pattern of increased and

decreased activation relative to baseline can be confirmed with trial-averaged BOLD signal for the

regions displayed in Figure 4a.

Discussion

FIR-CPCA was used to examine the temporal dynamics of functional networks involved in

verbal working memory. This technique involved performing principal component analysis on the

variation in BOLD signal that is predictable from a FIR model of the stimulus presentation timing. Four

components were extracted, all of which peaked at approximately 10 seconds following trials onset.

Two of the components sustained this peak for approximately 3 seconds (Components 1 and 4), and the

other two did not (Components 2 and 3). All components showed statistically significant sensitivity to

the memory load manipulation, and reliable HRF shapes.

It has recently been discovered that a wide range of effortful cognitive tasks consistently lead to

not only increases in activity in fronto-parietal brain regions but also concomitant decreases in activity

in ventro-medial brain regions. These anticorrelated networks have been coined the task-positive and

task-negative network, respectively (Fox, et al. 2005). The current network-focused analysis method

emphasized the possibility of an important interplay between the two anticorrelated functional

networks. Interestingly, most activations and deactivations observed in the current set of results can

understood within this context.

The exclusively negative component loadings on Component 1, combined with the BOLD signal

changes depicted in Figure 1c, suggest that activation decreased on initiation of a delayed recognition

trial. These deactivations included some task negative regions, such as posterior cingulate/precuneus

and superior medial prefrontal cortex. Also observed for this component was the coordinated decrease

in bilateral primary auditory cortex activity that could relate to reduced activation during inner speech

(Buchsbaum, et al. 2005; Frith, et al. 1991), or a more general phenomenon whereby task-irrelevant

primary sensory cortex (with visual cortex being task-relevant) is deactivated during task performance

(Laurienti, et al. 2002; Shulman, et al. 1997). The effect size associated with Component 1 was smallest

for the load 2 condition; however, it did not exhibit clearly linearly increasing load dependent

(de)activity. Together, the regions and patterns of activity for this component are consistent with

observations of task specific and non-specific deactivations related to working memory

Components 2 and 3 were dominated by regions typically involved in effortful, attention

demanding cognitive tasks in addition to those more specific to working memory, and both showed

clear load dependence, with linearly increasing effect sizes. Several of the neural regions involved in

both Components 2 and 3 appear consistent with the task-positive functional network, such as dorsal

anterior cingulate, postcentral/precentral gyri, and dorsolateral prefrontal cortex. Load-sensitive

involvement of fronto-parietal regions is also consistent with the multiple demands network of Duncan

et al. (Duncan and Owen 2000) in which these regions function as a network during the performance of

a variety of attention demanding tasks. Some of the observed regions have, however, been tied to more

specific roles in working memory. One of these, the fusiform gyrus, is considered sensitive to the

encoding and short-term maintenance of letter strings and words (Fiebach, et al. 2006). The superior

parietal lobule (Component 3) may play a critical role in both maintenance and manipulation of verbal

information in working memory, as demonstrated by a recent transcranial magnetic stimulation study

(Postle 2006), whereas the intraparietal sulcus is a candidate for capacity-limited storage in (visual)

working memory (Todd and Marois 2004). The posterior middle frontal gyrus (Components 2 and 3),

on the other hand, has been associated with control processes recruited during working memory

(Derrfuss, et al. 2004; McNab and Klingberg 2008). The visual cortices (BA 18, 19) were also strongly

activated but presumably reflect perception of visually presented stimuli during the initial phase of each

trial.

Component 4 was also strongly load dependent, and involved aspects of both the task positive

and task negative networks, and the fronto-parietal network. Relative to Components 2 and 3, the task-

positive aspects of Component 4 did not involve primary visual cortex regions, and included left inferior

prefrontal and right dorsolateral prefrontal activations that were more anterior than the like-lateralized

activations in Components 2 and 3. Relative to Component 1, the task-negative aspects of Component 4

were more anterior and dominant for the medial frontal regions, and more posterior and dominant

for the posterior cingulate and angular gyrus aspects.

It is perhaps important to comment upon the small amount of variance accounted for by

Component 4. Indeed, one might expect the task-positive processes sustained into the delayed

recognition trial to be more dominant, given that there are a number of processes related to memory

capacity limits, retrieval from memory, decision making, and response preparation/execution required

by the task, but it may be precisely the variability across these different processes which leads to the

relatively minor signal reflected by Component 4. Alternatively, or perhaps in addition to these reasons,

there could have been substantial individual differences within any of these processes resulting in

increased variability in the evoked signal. Some cognitive processes in which such individual

differences have been noted are proactive interference (Feredoes, et al. 2009), memory capacity (Todd

and Marois 2005), and the scanning of the contents of memory (Oztekin, et al. 2009). These

considerations of variability across subjects may help to constrain the interpretation of the processes

represented by the other components, in that they might be representing those processes which are less

susceptible to individual differences.

In sum, these networks revealed by FIR-CPCA are consistent with previous findings from both

the working memory literature and more general cognitive investigations. The identification of multiple

networks simultaneously is, however, a unique observation, and one would predict that with more

targeted manipulation of the different task stages, for example, the contribution of each network could

be more thoroughly explored.

Interpretation of Component Time Series.

All four components displayed peak activation approximately 10-11 seconds after trial onset,

which is precisely the peak expected for a HRF in response to a 3-second encoding stage. However,

only two of the four components sustained this peak activity, both for approximately 3 seconds

(Components 1 and 4). Although all components are likely invoked at encoding, the sustained peak

components are more likely to be involved in both the encoding and delay period.

Correspondingly, these sustained peak components may be more representative of the regions involved

in encoding *and* maintenance over a short period (Postle 2006).

Role of HRF shapes in FIR CPCA.

As was mentioned in the introduction, FIR models are preferable to HRF models in CPCA for a

number of reasons, one of which is avoidance of restricting the variance in *GC* to scaled versions of the

HRF model shapes. Given this, clarification may be needed to explain our reasons for revisiting HRF

models at the stage of component rotation. In this context, it is important to distinguish between the

three CPCA stages of analysis (Hunter and Takane 2002, p. 107-112): (1) the external analysis,

involving multivariate multiple regression, and depicted in Equations 1 and 3, (2) the internal analysis,

involving singular value decomposition, and depicted in Equations 2 and 4, and (3) component rotation,

depicted in Equations 5, 6 and 7. The internal analysis is exploratory in nature and does not involve use

of a FIR or HRF model. In contrast, the variance captured in the external analysis is completely

determined by the choice of model, such that any variation in BOLD signal that is not captured by the

model (e.g., that not conforming to a scaled version of the HRF model shapes) would be excluded for

the subsequent internal analysis, thus leading to the preference for the less restrictive FIR model. This

can be contrasted with the component rotation stage, which, as is clear from Equations 5, 6 and 7,

involves redistributing variance by creating weighted combinations of the existing columns of *VD*, *U*,

and *P* matrices. This allows new combinations of the patterns of variance contained in the components,

leading to new interpretations, but does not exclude certain patterns of variance as does the external

analysis, or create new patterns of to-be-redistributed variance. In fact, all rotations of the component

solution are equally valid, in that they don't change the adequacy of the solution; that is to say, the

percentage of variance in *GC* accounted for by the component solution will not change with rotation

methodology. Thus, the function of the HRF shapes at the rotation stage are to emphasize HRF-shaped

patterns that already exist in the component solution, but not to increase or decrease the

percentage of variance accounted for by the component solution.

Comparison to Prior Analyses.

Our original CPCA analysis of these data (Woodward, et al. 2006) used a design matrix in *G*,

which modeled stage-specific hemodynamic responses as idealized BOLD responses to stimulus

presentations. The current FIR model method allowed the following to be demonstrated: (1) a load-

dependent interpretation for a previously uninterpretable component; namely, a deactivated network

likely involved in encoding and delay period processes (Component 1); (2) a detailed display of the

estimated hemodynamic response associated with each component; (3) elimination of the risk of

interpretative errors linked to inaccurately labeled or inaccurately derived hemodynamic response

models of correlated task stages; and (4) elimination of the risk that BOLD activity not conforming to

the modeled synthetic HRF shape is either misattributed to correlated task stages, or is overlooked by

the analysis procedure.

As a concrete example of how the FIR-CPCA analysis can eliminate the risk of certain

interpretative errors, we revisit our previous paper (Woodward, et al. 2006) where we reported evidence

for a "load-dependent, reciprocal relationship" between the encoding and delay networks that involved

the occipital cortex (based on a component similar to what is referred to here as Component 4). In light

of the results obtained from the FIR analysis, our previous interpretation appears erroneous. The

previously reported component displayed negative component loadings in occipital regions along with

task-positive activations (and reciprocal task-negative deactivations), which did not replicate in the FIR

analysis. The FIR analysis clarifies that both actually increased with the onset of encoding, with the

visual cortex activation (Component 2 and 3) dropping off earlier than the task-positive activations (and

task negative deactivations) on Component 4. This suggests that the previously reported negative

component loadings in occipital regions were due to spurious correlations between a decrease in

occipital cortex due to termination of the visual display, and task-related deactivations associated with

the task-negative network. The emergence of these predictor weights, and the misinterpretation

of occipital decreases associated with the termination of the encoding display as deactivations

associated with the delay period (and reciprocally related to encoding), appear to be interpretational

errors partly caused by the false precision associated with using labels attached to HRF models of task

stages.

Comparison of CPCA to related Multivariate Methods

There are a number of previously proposed multivariate methods for analyzing fMRI data that

examine the relationship between two sets of variables (*X* and *Y*, denoting stimulus information and

BOLD signal, respectively), such as PLS (McIntosh, et al. 2004), CVA (Strother, et al. 2004), and

MLM (Worsley, et al. 1997). Although these approaches are similar to CPCA, and are mathematically

equivalent under some conditions, there are some important differences.

One of the main considerations when comparing CPCA to other multivariate approaches relates

to the fit between the statistical method and the logic underlying fMRI experiments, with respect to how

the *X* and *Y* matrices are placed on the predictor and/or criterion sides of the general linear model. Most

fMRI experiments, such as the current one, are designed to determine how experimental design and

stimulus timing (modeled in *X* and treated as a fixed effect) affects the distribution of the brain state (as

measured by the BOLD signal *Y*); therefore, information about the stimulus presentations should be

considered a set of predictor variables, and the BOLD signal a set of criterion variables. Regression

analysis specifically analyzes the conditional expectation of Y given X, that is to

say, $E(Y \mid X) = \int (Yp(Y \mid X))dX$, where $p(Y \mid X)$ is the (conditional) distribution of Y given X.

Correspondingly, for CPCA, *X* is placed on the predictor side, *Y* is placed on the criterion side, and the

objective is to find a consequence of *X*, which is, in turn, a cause for *Y*, thereby providing a natural fit to

the logic underlying typical fMRI experimental designs. For CPCA (or any linear regression analysis)

$E(Y \mid X)$ is assumed linear. In other contexts, however, the motivation may be to predict stimulus

condition X from the brain state Y, as is the case with mind-reading paradigms (Hansen 2007), for

which discriminant function analysis would be a more appropriate analytic method (review of this class

of fMRI experiments is outside the scope of the current discussion, but please refer to Haynes and Rees

2006).

In contrast to CPCA, PLS places both X and Y on the criterion side and seeks to find a common

cause for both. The mathematical technique employed by PLS is commonly referred to as least squares

inter-battery factor analysis (Tucker 1958), where it is assumed that there is a common cause for the two

sets of variables and their joint distribution is analyzed (Hansen 2007). This is the methodology of

choice under conditions where neither X nor Y are controlled. However, it should be noted that PLS

reduces to a special case of CPCA when X is column-wise orthonormal.

Despite this mathematical equivalence, the current application of CPCA would not give the

same results as the PLS software package (McIntosh, et al. 2004) due to important differences in the

matrices submitted to the analysis. For example, in PLS, the BOLD signal matrix referred to above as Y

is converted to a percent signal change (from trial onset) and reorganized into a matrix that the authors

referred to as M. Each row of the M matrix contains the (percent-signal-change converted) BOLD signal

from pre-specified peristimulus time points, averaged over all occurrences of the condition of interest,

computed separately for each subject and condition. Thus, unlike its CPCA counterpart Z, M will not

consider BOLD signal from the entire time series if the specified number of scans comprising

peristimulus time does not cover all collected scans due to the experiment design. (The CPCA method

of using the values 0 and 1 in G to contrast peristimulus time against other scans in Z does not have the

same effect as the PLS method of selecting only scans in peristimulus time for inclusion in M. G is used

as a set of binary predictor variables in a multivariate multiple regression, and the actual values are

arbitrary and do not affect results.) An additional difference involves the matrix representing the

experimental design, referred to above as X, but referred to as C by the authors. Unlike its CPCA

counterpart G, the PLS-based C does not contain a model of the hemodynamic response, but instead

contains codes that contrast the averaged BOLD signal from the conditions represented in the

rows of *M*.

CVA is a special case of canonical correlation analysis, where it is assumed that the two sets of

variables are causing a common factor, typically arising when *X* and *Y* are causing something in

common. As such, CVA places both *X* and *Y* on the predictor side, and seeks to find a common

consequence of both. In the case where *Y* is column-wise orthonormal, or *X* is a matrix of dummy

variables indicating class labels, CVA reduces to CPCA. However, in part due to due to the preliminary

PCA performed on the BOLD signal, CVA as suggested by Strother et al. (2004) would not match the

results provided by the current application of CPCA.

In MLM, as in CPCA, *X* is placed on the predictor side, and *Y* is placed on the criterion side, and

the objective is to find a consequence of *X*, which is, in turn, a cause for *Y*. In terms of mathematical

operations, the main difference between MLM and CPCA lies in the estimation method they use. MLM

uses a heuristic estimation method, which is claimed to be robust, and leads to an analytical significance

testing procedure (Worsley, et al. 1997), and takes into account possible nonzero covariances among the

rows of *Z* represented by a matrix *S*. The estimation method used in CPCA is consistent with

redundancy analysis (Lambert, et al. 1988), and in the form utilized here, it ignores the covariances

among the rows of *Z*; however, this could be remedied by taking $C = (G'S^{-1}G)^{-1}G'S^{-1}Z$ as the rank-

free estimate of regression weights (rather than assuming *S = I*), where *S* is the covariance matrix among

the rows of *Z*. If *S* is known exactly (i.e., when the population covariance matrix is known), this gives

the best linear unbiased estimator (BLUE) of *C*. *S* usually has to be estimated, however, and a very good

estimate of *S* must exist in order for the above estimator to work well, and this is also the case for

MLM. In general, it is difficult to determine which estimation method (MLM or CPCA) is uniformly

better than the other in a small sample, and this question must be addressed empirically in future

research.

As a final and very important point of comparison, CPCA provides a more general

mathematical framework than PLS, CVA or MLM, in that it allows the data to be decomposed into

sources of variance predictable from row information (as does PLS, CVA or MLM), but also from

column information, contrasts of row and column information, all combinations thereof, as well as the

variance *not* explained by row or column information, with components being computed on any or all of

those sources of variance (Takane and Hunter 2001; Takane and Shibayama 1991). The full CPCA

model is as follows:

$$Z = GMH' + BH' + GC + E \ , \hspace{2cm} (8)$$

With the *H* matrix providing constraints on the voxels coded in the columns of *Z*, and *GMH* is variance

in *Z* predictable from the interaction between *G* and *H*. We are currently developing applications of

CPCA to use the *G* and *H* matrices simultaneously to analyze fMRI data. Candidates for the *H* matrix

are anatomical networks of theoretical interest, such ventral/dorsal networks, lateralization of cognitive

functions, or any a priori neural networks of interest.

Conclusions

This FIR-CPCA analysis methodology provided a method for assessing functional connectivity

between neural regions engaged by a verbal delayed recognition task. This approach allowed (1)

determination of multiple functional networks involved in working memory, (2) estimation of the

pattern of BOLD changes associated with each functional network over peristimulus time points, (3) a

statistical test of the reliability of the HRF associated with each component; and (4) a statistical test of

the degree to which experimental manipulations (in this case working memory load) affects each

functional network. Each of the components included brain regions consistent with previous studies on

the stages involved in working memory delayed recognition, but also included regions involved in the

putative task-positive/task-negative anticorrelated functional networks (Fox, et al. 2005) and the

multiple demands network (Duncan and Owen 2000). The ability to visualize the pattern of activity of a

CPCA 26

correlated network over time, and its sensitivity to experimental manipulations, is suited

particularly to investigation of multiple-stage cognitive tasks.

References

Baddeley AD, Hitch GJ. 1974. Working Memory. In: Bower GA, editor. The psychology of learning

and motivation: advances in research and theory. New York: Academic Press. p 47-89.

Buchsbaum BR, Olsen RK, Koch PF, Kohn P, Kippenhan JS, Berman KF. (2005): Reading, hearing,

and the planum temporale. Neuroimage 24(2):444-54.

Cairo TA, Liddle PF, Woodward TS, Ngan ETC. (2004): The influence of working memory load on

phase specific patterns of cortical activity. Cognitive Brain Research 21:377-387.

Cairo TA, Woodward TS, Ngan ET. (2006): Decreased encoding efficiency in schizophrenia. Biological

Psychiatry 59(8):740-6.

Calhoun VD, Adali T, Stevens MC, Kiehl KA, Pekar JJ. (2005): Semi-blind ICA of fMRI: A method

for utilizing hypothesis-derived time courses in a spatial ICA analysis. Neuroimage 25(2):527-

38.

Dale AM. (1999): Optimal experimental design for event-related fMRI. Hum Brain Mapp 8(2-3):109-

14.

Dale AM, Buckner RL. (1997): Selective averaging of rapidly presented individual trials using fMRI.

Human Brain Mapping 5:329-340.

Derrfuss J, Brass M, von Cramon DY. (2004): Cognitive control in the posterior frontolateral cortex:

evidence from common activations in task coordination, interference control, and working

memory. Neuroimage 23(2):604-612.

Duncan J, Owen AM. (2000): Common regions of the human frontal lobe recruited by diverse cognitive

demands. Trends in Neurosciences 23(10):475-483.

Feredoes E, Tononi G, Postle BR. (2009): Prefrontal Control of Familiarity and Recollection in

Working Memory. Journal of Cognitive Neuroscience.

Fiebach CJ, Rissman J, D'Esposito M. (2006): Modulation of Inferotemporal Cortex Activation during

Verbal Working Memory Maintenance. Neuron 51(2):251-261.

CPCA 28

Fox MD, Snyder AZ, Vincent JL, Corbetta M, Van Essen DC, Raichle ME. (2005): The human

brain is intrinsically organized into dynamic, anticorrelated functional networks. Proceedings of

the National Academy of Sciences USA 102(27):9673-8.

Frith CD, Friston KJ, Liddle PF, Frackowiak RS. (1991): A PET study of word finding.

Neuropsychologia 29(12):1137-1148.

Glover GH. (1999): Deconvolution of impulse response in event-related BOLD fMRI. Neuroimage

9(4):416-429.

Hansen LK. (2007): Multivariate strategies in functional magnetic resonance imaging. Brain and

Language 102(2):186-191.

Harman HH. 1967. Modern Factor Analysis. Chicago: The University of Chicago Press.

Haynes JD, Rees G. (2006): Decoding mental states from brain activity in humans. Nat Rev Neurosci

7(7):523-34.

Henson R, Rugg MD, Friston K. (2001): The choice of basis functions in event-related fMRI.

NeuroImage 13(6):s149.

Hunter MA, Takane Y. (2002): Constrained principal component analysis: Various applications. Journal

of Educational and Behavioral Statistics 27(2):105-145.

Lambert ZV, Wildt AR, Durand RM. (1988): Redundancy analysis: An alternative to canonical

correlation and multivariate multiple regression in exploring interset associations. Psychological

Bulletin 104(2):282-289.

Laurienti PJ, Burdette JH, Wallace MT, Yen YF, Field AS, Stein BE. (2002): Deactivation of sensory-

specific cortex by cross-modal stimuli. J Cogn Neurosci 14(3):420-9.

Manoach DS, Greve DN, Lindgren KA, Dale AM. (2003): Identifying regional activity associated with

temporally separated components of working memory using event-related functional MRI.

Neuroimage 20(3):1670-1684.

McIntosh AR, Chau WK, Protzner AB. (2004): Spatiotemporal analysis of event-related fMRI

data using partial least squares. Neuroimage 23(2):764-775.

McKeown MJ, Makeig S, Brown GG, Jung TP, Kindermann SS, Bell AJ, Sejnowski TJ. (1998):

Analysis of fMRI data by blind separation into independent spatial components. Hum Brain

Mapp 6(3):160-88.

McNab F, Klingberg T. (2008): Prefrontal cortex and basal ganglia control access to working memory.

Nature Neuroscience 11(1):103-7.

Ollinger JM, Corbetta M, Shulman GL. (2001): Separating processes within a trial in event-related

functional MRI I. The Method. NeuroImage 13(1):210-217.

Oztekin I, McElree B, Staresina BP, Davachi L. (2009): Working memory retrieval: contributions of the

left prefrontal cortex, the left posterior parietal cortex, and the hippocampus. Journal of

Cognitive Neuroscience 21(3):581-93.

Pedhazur EJ. 1982. Multiple regression in behavioral research: Explanation and Prediction. Toronto:

Holt, Rinehart and Winston.

Penny WD, Stephan KE, Mechelli A, Friston KJ. (2004): Modelling functional integration: a

comparison of structural equation and dynamic causal models. Neuroimage 23 Suppl 1:S264-74.

Postle BR. (2006): Working memory as an emergent property of the mind and brain. Neuroscience

139(1):23-38.

Postle BR, Zarahn E, D'Esposito M. (2000): Using event-related fMRI to assess delay-period activity

during performance of spatial and nonspatial working memory tasks. Brain Res Brain Res

Protoc 5(1):57-66.

Serences JT. (2004): A comparison of methods for characterizing the event-related BOLD timeseries in

rapid fMRI. Neuroimage 21:1690-1700.

Shulman GL, Corbetta M, Buckner RL, Raichle ME, Fiez JA, Miezin FM, Petersen SE. (1997): Top-

down modulation of early sensory cortex. Cereb Cortex 7(3):193-206.

Strother S, La Conte S, Kai Hansen L, Anderson J, Zhang J, Pulapura S, Rottenberg D. (2004): Optimizing the fMRI data-processing pipeline using prediction and reproducibility performance metrics: I. A preliminary group analysis. Neuroimage 23 Suppl 1:S196-207.

Takane Y, Hunter MA. (2001): Constrained principal component analysis: A comprehensive theory. Applicable Algebra in Engineering, Communication and Computing 12:391-419.

Takane Y, Shibayama T. (1991): Principal component analysis with external information on both subjects and variables. Psychometrika 56(1):97-120.

Todd JJ, Marois R. (2004): Capacity limit of visual short-term memory in human posterior parietal cortex. Nature 428(6984):751-4.

Todd JJ, Marois R. (2005): Posterior parietal cortex activity predicts individual differences in visual short-term memory capacity. Cogn Affect Behav Neurosci 5(2):144-55.

Tucker LR. (1958): An inter-battery method of factor analysis. Psychometrika 23(2):111-136.

Viviani R, Gron G, Spitzer M. (2005): Functional principal component analysis of fMRI data. Human Brain Mapping 24(2):109-129.

Woodward TS, Cairo TA, Ruff CC, Takane Y, Hunter MA, Ngan ETC. (2006): Functional connectivity reveals load dependent neural systems underlying encoding and maintenance in verbal working memory. Neuroscience 139(1):317-325.

Worsley K, Poline J, Friston K, Evans A. (1997): Characterizing the response of PET and fMRI data using multivariate linear models. NeuroImage 6:305-319.

Yates A. 1987. Multivariate exporatory data analysis: A perspective on exploratory factor analysis. Albany: State University of New York Press.

Zarahn E, Aguirre G, D'Esposito M. (1997): A trial-based experimental design for fMRI. Neuroimage 6(2):122-138.

Acknowledgments

Table 1. Anatomical descriptions for each cluster (> 5 voxels) of Component 1, with corresponding Brodmann's Areas and peak Talairach (XYZ) coordinates. Bold type denotes the region with the maximum loading for that cluster.

Cortical Region	Brodmann's Area	Max Talairach Coordinate
Cluster 1: right hemisphere		
Superior Temporal Gyrus	**22**	**51 -8 -10**
Insula		36 0 4
Middle Temporal Gyrus	21	51 -8 -13
Angular Gyrus	39	48 -53 28
Cluster 2: left hemisphere		
Supramarginal Gyrus	**40**	**-55 -49 28**
Heschl's Gyrus	41/42	-36 -30 16
Superior Temporal Gyrus	22	-44 -34 16
Middle Temporal Gyrus	21	-48 -58 14
Cluster 3: bilateral		
Precuneus	**7**	**8 -65 25**
Posterior Cingulum	23	8 -37 39
Postcentral Gyrus	3	-20 -32 61
Supplementary Motor Cortex	6	-8 -17 49
Cluster 4: right hemisphere		
Superior Frontal Gyrus	**9**	**20 33 39**
Middle Frontal Gyrus	9	24 33 39
Inferior Frontal Gyrus (pars opercularis)	46	32 17 36
Cluster 5: left hemisphere		
Postcentral Gyrus	**3**	**-20 -32 61**
Precentral Gyrus	4	-12 -29 46
Cluster 6: left hemisphere		
Middle Frontal Gyrus	**8**	**-28 18 43**
Cluster 7: left hemisphere		
Paracingulate Gyrus	**32**	**-12 48 27**
Superior Frontal Gyrus	9	-12 52 27
Cluster 8: left hemisphere		
Postcentral Gyrus	**3**	**-32 -21 42**
Cluster 9: left hemisphere		
Middle Frontal Gyrus	**9**	**-24 33 35**
Cluster 10: right hemisphere		
Precentral Gyrus	**3**	**51 -14 27**
Postcentral Gyrus		

Table 2. Anatomical descriptions for each cluster (> 5 voxels) of Component 2, with corresponding Brodmann's Areas and peak Talairach (XYZ) coordinates. Bold type denotes the region with the maximum loading for that cluster.

Cortical Region	Brodmann's Areas	Max Talairach Coordinate
Cluster 1: bilateral		
Fusiform Gyrus	**19**	**28 -82 -13**
Middle Occipital Gyrus	18	32 -89 8
Lingual Gyrus	17	16 -82 13
Inferior Occipital Gyrus	18	24 -82 13
Cluster 2: bilateral		
Precuneus	**7**	**-8 -75 48**
Cuneus	19	-4 -80 33
Cluster 3: left hemisphere		
Cerebellum		**-36 -75 -16**
Fusiform Gyrus	19	-40 -74 -13
Middle Occipital Gyrus	19	-48 -70 -10
Inferior Occipital Gyrus	19	-44 -82 -6
Cluster 4: bilateral		
Medial Frontal Gyrus	**6**	**0 3 59**
Superior Frontal Gyrus	6	4 7 62
Middle Frontal Gyrus	6	32 -1 55
Precentral Gyrus	4	28 -16 63
Cluster 5: left hemisphere		
Superior Frontal Gyrus	**6**	**-32 -8 63**
Middle Frontal Gyrus		-32 -5 59
Precentral Gyrus		-32 -9 59
Cluster 6: left hemisphere		
Middle Frontal Gyrus	**6**	**-51 2 40**
Postcentral Gyrus	3	-51 -9 45
Precentral Gyrus	4	48 -9 48
Cluster 7: bilateral		
Thalamus		**-8 -11 12**
Cluster 8: left hemisphere		
Cuneus	**17**	**-16 -93 -2**
Lingual gyrus	18	-8 -93 1
Cluster 9: bilateral		
Cerebellum		**4 -47 2**
Cluster 10: right hemisphere		
Subcallosal Gyrus / Gyrus Rectus	**11**	**16 19 -11**
Putamen		16 11 -7

Cluster 11: left hemisphere		
Cerebellum		**-28 -59 -14**
Cluster 12: bilateral		
Thalamus		**0 -27 5**
Cluster 13: left hemipshere		
Superior Temporal Gyrus	**22**	**-59 11 -4**

Table 3. Anatomical descriptions for each cluster (> 5 voxels) of Component 3, with corresponding Brodmann's Areas and peak Talairach (XYZ) coordinates. Bold type denotes the region with the maximum loading for that cluster.

Cortical Region	Brodmann's Area	Max Talairach Coordinate
Cluster 1: right hemisphere		
Lingual Gyrus	**18**	**16 -82 -6**
Middle Occipital Gyrus	19	28 -69 26
Superior Lateral Occipital Cortex	7	24 -63 51
Superior Parietal Lobule	7	32 -56 51
Cluster 2: left hemisphere		
Middle Occipital Gyrus	**19**	**-32 -81 19**
Superior Lateral Occipital Cortex	18	-24 -84 26
Occipital Pole	17	-8 -93 -2
Intracalcarine Cortex	17	-12 -81 4
Cluster 3: left hemisphere		
Posterior Inferior Temporal Gyrus	**37**	**-44 -63 -14**
Temporal Occipital Fusiform Cortex	37	-40 -59 -14
Superior Lateral Occipital Cortex	19	-44 -67 -13
Occipital Fusiform Gyrus	19	-36 -67 -17
Cluster 4: left hemisphere		
Superior Parietal Lobe	**7**	**-28 -60 47**
Superior Lateral Occipital Cortex	7	-20 -68 48
Cluster 5: left hemisphere		
Precentral Gyrus	**4**	**-51 -6 44**
Cluster 6: right hemisphere		
Middle Frontal Gyrus	**46**	**40 40 27**
Cluster 7: bilateral		
Paracingulate Gyrus	**32**	**0 14 47**
Posterior Superior Frontal Gyrus	6	0 14 55
Cluster 8: right hemisphere		
Precentral Gyrus	**6**	**55 9 33**
Inferior Frontal Gyrus (pars opercularis)	44	48 9 22
Cluster 9: left hemisphere		
Supramarginal Gyrus	**40**	**-40 -45 32**
Cluster 10: left hemisphere		
Inferior Frontal Gyrus (pars opercularis)	**44**	**-51 13 18**

Table 4. Anatomical descriptions for each cluster (> 5 voxels) of Component 4, with corresponding Brodmann's Areas and peak Talairach (XYZ) coordinates. Bold type denotes the region with the maximum loading for that cluster.

Cortical Region	Brodmann's Areas	Max Talairach Coordinate
Positive Component loadings		
Cluster 1: bilateral		
Medial Frontal Gyrus	**6**	**-4 -1 55**
Superior Frontal Gyrus	6	-8 10 47
Precentral Gyrus	6	-36 -5 52
Inferior Frontal Gyrus	44	-51 5 26
Cluster 2: left hemisphere		
Inferior Frontal Gyrus	**47**	**-36 23 -5**
Middle Frontal Gyrus	45	-44 32 13
Insula		-40 12 3
Cluster 3: left hemisphere		
Middle Occipital Gyrus	**19**	**-28 -69 26**
Superior Occipital Gyrus	19	-20 -64 33
Cluster 4: right hemisphere		
Middle Frontal Gyrus	**46**	**32 47 16**
Superior Frontal Gyrus	46	24 48 20
Cluster 5: left hemisphere		
Middle Occipital Gyrus	**37**	**-48 -63 -7**
Cluster 6: left hemisphere		
Supramarginal Gyrus	**40**	**-40 -41 35**
Negative Component loadings		
Cluster 1: bilateral		
Superior Frontal Gyrus	**10**	**8 60 26**
Medial Frontal Gyrus	9	-4 56 34
Anterior Cingulum	32	4 47 9
Cluster 2: left hemisphere		
Angular Gyrus	**39**	**-48 -68 37**
Middle Occipital Gyrus	19	-40 -76 33
Middle Temporal Gyrus	21	-55 -61 22
Cluster 3: right hemisphere		
Angular Gyrus	**39**	**48 -60 44**
Middle Temporal Gyrus	21	55 -61 21
Supramarginal Gyrus	40	59 -49 28
Cluster 4: bilateral		

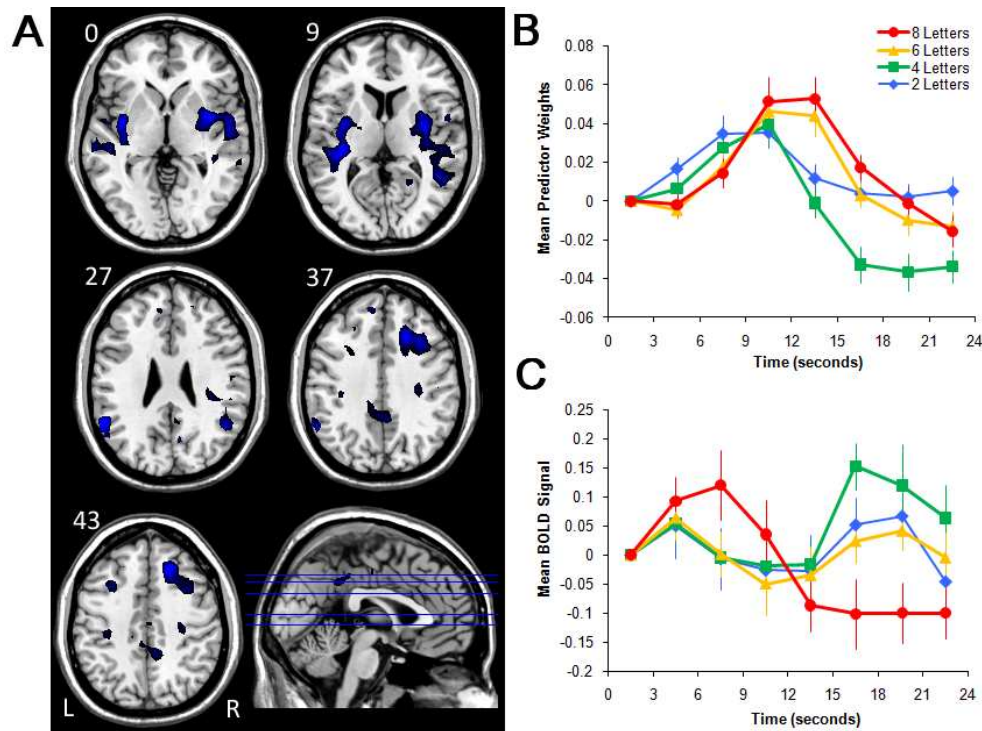|		
Precuneus	**23**	**4 -57 32**
Posterior Cingulum	23	0 -53 28
Cuneus		0 -69 26
Cluster 5: left hemisphere		
Anterior Cingulum	**32**	**-16 44 16**
Cluster 6: left hemisphere		
Superior Frontal Gyrus	**46**	**-28 59 15**

Figure 1. Images, plots of predictor weights, and plots of BOLD signal for Component 1. The dominant 5% of component loadings are displayed (A), with negative component loadings displayed in black (max = -.32) and blue (min = -.39). (No positive component loadings passed this threshold.) The mean FIR-based predictor weights are plotted as a function of perstimulus time in the right panel, top (B; error bars are standard errors). The predictor weights at the first point of peristimulus time are adjusted to zero, and all other values scaled accordingly for each subject, and therefore differ from % signal change by a constant term only. The mean BOLD signal extracted from the regions displayed in (A) are plotted as a function of perstimulus time in the right panel, bottom (C; error bars are standard errors). Axial slices are located at the following Talairach z axis coordinates: 0, 9, 27, 37, 43.
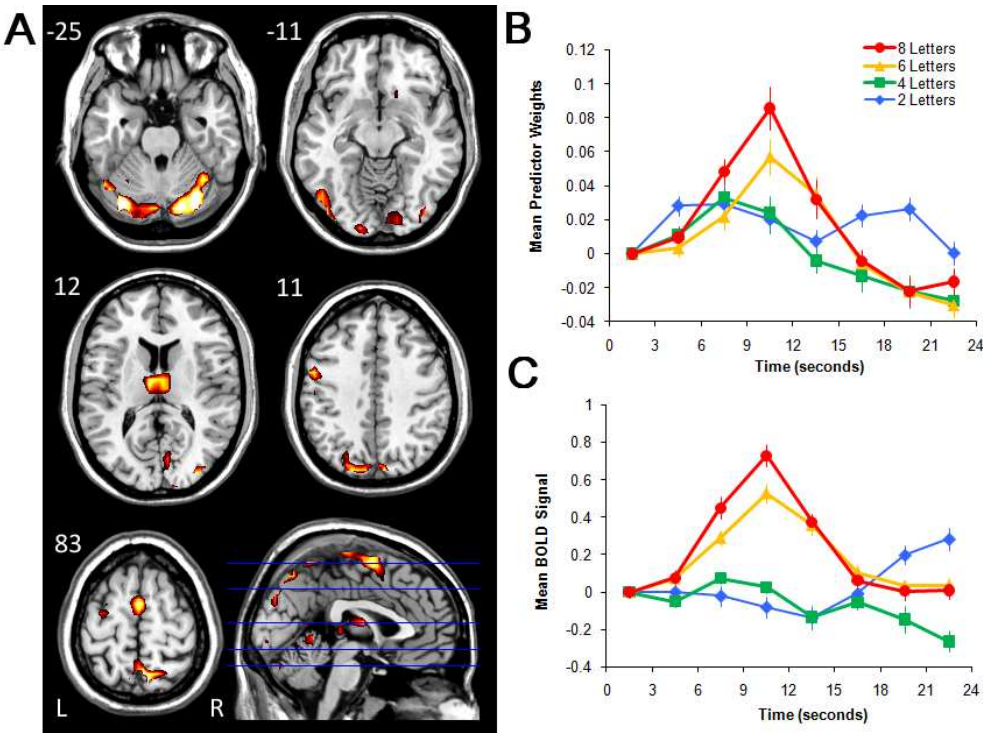
Figure 2. Images, plots of predictor weights, and plots of BOLD signal for Component 2. The dominant 5% of component loadings are displayed (A), with positive component loadings displayed in red (min = .26) and yellow (max = .41). (No negative component loadings passed this threshold.) The mean FIR-based predictor weights are plotted as a function of perstimulus time in the right panel, top (B; error bars are standard errors). The predictor weights at the first point of peristimulus time are adjusted to zero, and all other values scaled accordingly for each subject, and therefore differ from % signal change by a constant term only. The mean BOLD signal extracted from the regions displayed in (A) are plotted as a function of perstimulus time in the right panel, bottom (C; error bars are standard errors). Axial slices are located at the following Talairach z axis coordinates: -25, -11, 12, 11, 83.
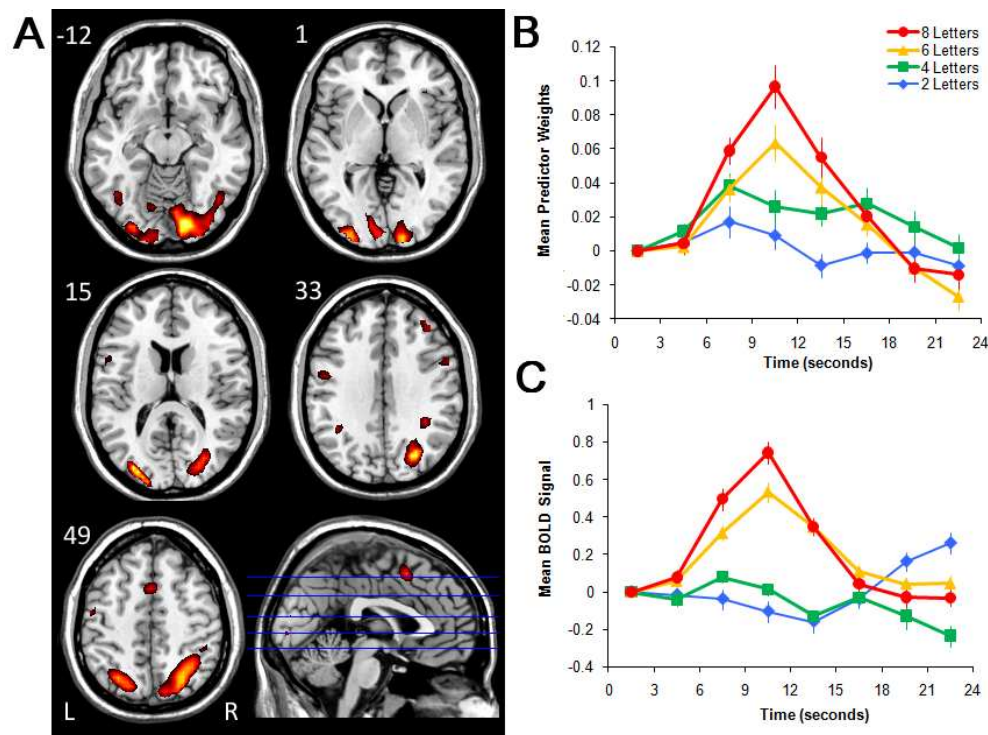
Figure 3. Images, plots of predictor weights, and plots of BOLD signal for Component 3. The dominant 5% of component loadings are displayed (A), with positive component loadings displayed in red (min = .26) and yellow (max = .41). The predictor weights at the first point of peristimulus time are adjusted to zero, and all other values scaled accordingly, and therefore differ from % signal change by a constant term only. The mean FIR-based predictor weights are plotted as a function of peristimulus time in the right panel, top (B). The mean BOLD signal extracted from the regions comprising the FIR component positive component loadings are plotted in the right panel, bottom (C), and the negative component loadings are plotted in the bottom panel (D; error bars are standard errors). Axial slices are located at the following Talairach z axis coordinates: -12, 1, 15, 33, 49.

1
2
3
4
5
6
7
8
9
10
11
12
13
14
15
16
17
18
19
20
21
22
23
24
25
26
27
28
29
30
31
32
33
34
35
36
37
38
39
40
41
42
43
44
45
46
47
48
49
50
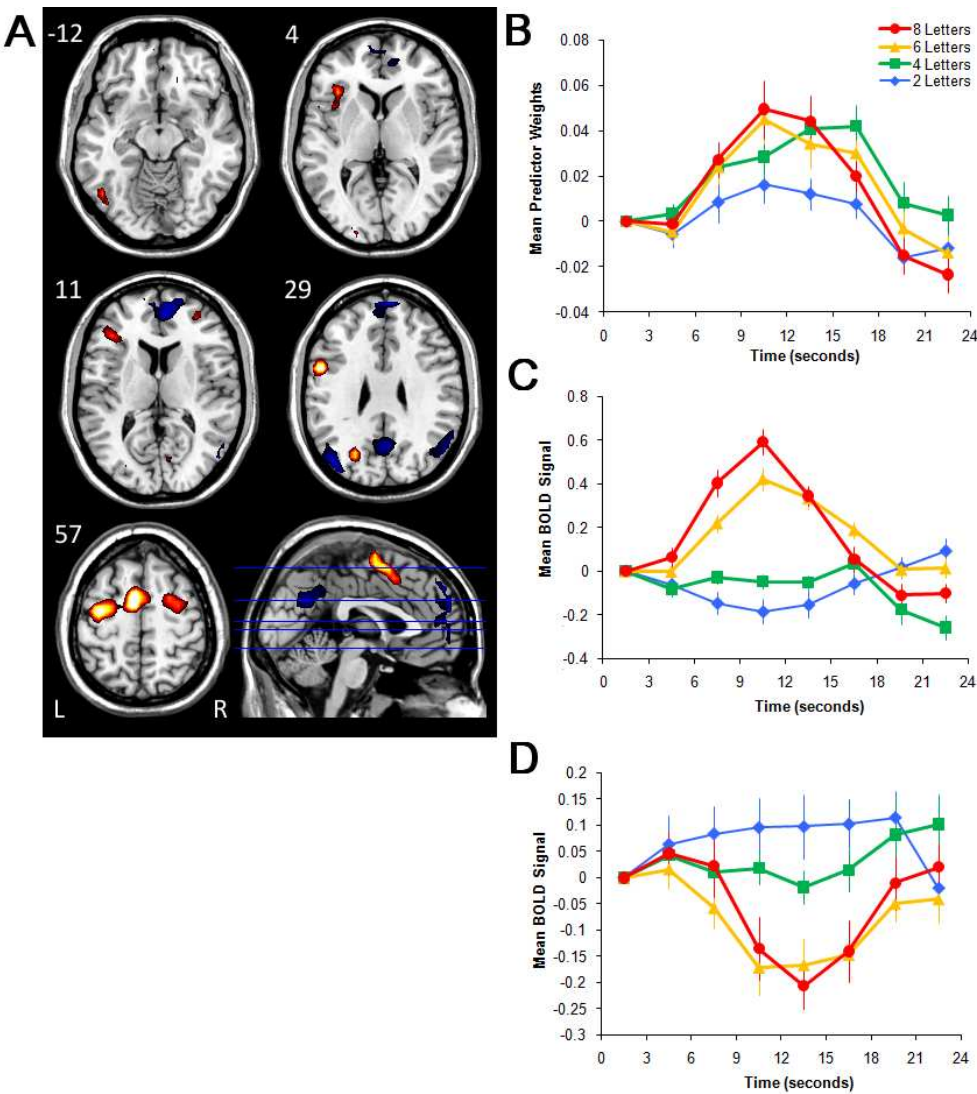51
52
53
54
55
56
57
58
59
60

Figure 4. Images, plots of predictor weights, and plots of BOLD signal for Component 4. The dominant 5% of component loadings are displayed (A), with positive component loadings displayed in red (min = .17) and yellow (max = .29), and negative component loadings are displayed in black (max = -.17) and blue (min = -.30). The predictor weights at the first point of peristimulus time are adjusted to zero, and all other values scaled accordingly, and therefore differ from % signal change by a constant term only. The mean FIR-based predictor weights are plotted as a function of peristimulus time in the right panel, top (B). The mean BOLD signal extracted from the regions comprising the FIR component positive component loadings are plotted in the right panel, bottom (C), and the negative component loadings are plotted in the bottom panel (D; error bars are standard errors). Axial slices are located at the following Talairach z axis coordinates: -12, 4, 11, 29, 57.